Addendum to Application for Incidental Harassment Authorization for the Non-Lethal Taking of Whales and Seals in Conjunction with a Proposed Seismic Survey in the Beaufort Sea, Alaska, Summer 2008

May 2008

Prepared for

PGS Onshore, Inc.
3201 C Street, Suite 403
Anchorage, Alaska 99503

Prepared by

ASRC Energy Services
a subsidiary of Arctic Slope Regional Corporation
Regulatory and Technical Services

3900 C Street, Suite 601
Anchorage, Alaska 99503

Table of Contents

List of Figures

List of Appendices

ACRONYMS

bar-m	bar meters
cu in	cubic inches
cu m	cubic meter(s)
dB	decibels
ft	foot/feet
Hz	hertz
m	meter(s)
M/V	marine vessel
NMFS	National Marine Fisheries Service
PGS	PGS Onshore, Inc.
rms	root mean square
re 1 μPa-m	relative to one microPascal at one meter distant

1.0 INTRODUCTION

PGS Onshore, Inc., (PGS) has been contracted by ENI Petroleum (ENI) to conduct an exploratory three-dimensional (3D) marine seismic survey in the Beaufort Sea of Alaska, utilizing an ocean bottom cable/ transition zone technique.

This Addendum was created to provide additional information as requested by the National Marine Fisheries Service as part of the review of the Incidental Harassment Authorization (IHA) application submitted to NMFS by PGS on May 9, 2008.

2.0 SAFETY RADII AND MODELING

2.1 Sources Used for Data Acquisition

PGS will use two source vessels, marine vessel (M/V) *Wiley Gunner* and M/V *Little Joe*, which will both be equipped with identical airgun arrays with a total air discharge volume of 0.014 cubic meters (cu m) (880 cubic inches [cu in]). Each array will be made up of four 0.00164 cu m (100 cu in) airguns and six 0.00131 (80 cu in) airguns, configured as shown in Figure 1. The airguns comprising the arrays are smaller than most arrays used in seismic programs in either the Beaufort Sea or Chukchi Sea, and are expected to operate at a depth of between 0.91 meters (m) and 2.29 m (3 feet [ft] and 7.5 ft).

2.2 Modeling Technique

The airgun array was modeled using Nucleus Marine Source Modeling software, which is a software program typical of that used though out the seismic industry. The modeling software includes source interaction effects, directivity considerations, and attenuation with distance. The method used for the model is detailed in the attached technical paper *The QCD Modeling Scheme*.

The software is set up to calculate the resulting wavelet for any distance or direction from an arrayed source. The Farfield signature thus obtained is normalized to a distance of one meter. The wavelet is injected into an earth model composed of a group of cells. The air layer, water layer, and sediment layer are explicitly defined. Each cell is assigned velocities and densities and the wave equation is evaluated at the appropriate number of cells to simulate propagation of the wave through the model. This software includes transmission, reflection, refraction, absorption, waveform interaction, and spectral decay evaluation.

Conventional decibel (dB) scales used to compare marine seismic source arrays are in units of dB relative to 1 micro Pascal at 1 meter per Hertz (dB re 1 µPa-m /Hz). The "per Hertz" notation indicates however that this measurement should be taken in the frequency domain, **not in the time domain.** Time domain measurements are typically noted in bar-meters.

The PGS source has a peak to peak amplitude equal to 31.4 bar-meters (bar-m)using the time domain Farfield signature (Figure 2). The direct conversion to dB would give a source output of 249.94 dB:

$20 \log10(\text{bar-m}*10^{11}) = \text{dB}$

$20 \log10(31.4*10^{11}) = 249.94 \text{ dB}$

However this source strength is not conventionally used in the industry when comparing relative strengths of marine seismic source arrays, as it has been generated using amplitude in the time domain**,** and not the frequency domain.

To resolve this and get an accurate measurement of absolute dB for the air gun source, the time signature is processed using a Fourier Transform to obtain the amplitude and phase spectra of the signature. The resulting amplitude spectra is then converted to dB utilizing the formula above, resulting in the Frequency Domain Measurement (Figure 3) which details absolute dB through the graphed frequency ranges. In the case of the 880 cu in the source proposed by PGS, the maximum absolute dB is slightly less than 200 dB at a frequency between 40 and 50 Hz.

2.3 Sound Source Results

Model results indicate that the maximum amplitude is 197 dB dB re 1 μPa-m (peak) at 42 Hz. Therefore the modeled sound level at source is 192.7 dB re 1 μPa-m root mean square (rms) at frequencies between about 10 Hz and 100 Hz. The absolute dB decreases at frequencies higher than 100 Hz as shown on Figure 3.

2.4 Sound Propagation

The proposed PGS array is specifically designed to direct sound pressure downwards as shown in Figures 4 and 5. Figure 4 shows an inline (bow to stern) cross section maximum amplitude in dB; Figure 5 shows a crossline (port to starboard) crossline cross section maximum amplitude in dB. Sound propagation is quickly attenuated through interference patterns between the individual guns on the array. Based upon the model, the radii distance to the 190-dB isopleth is only a couple of meters (6 to 9 ft), while the distance to the 180-dB isopleth is only about 10 m (30 ft). As shown on Figure 5, inline maximum amplitude reduces to 160 dB in less than 40 m (130 ft). Crossline maximum amplitude reduces to 160 dB in approximately 35 m (115 ft) (Figure 7).

Monitoring a 10-m (30-ft) safety radii is impractical. Therefore, PGS is proposing to establish a more conservative 50-m (160-ft) safety radii centered over the array. Establishing a shutdown safety radius of 50 m (160 ft) for all marine mammals, the most conservative estimate for the 180-dB isopleth, should ensure injurious "takes" are avoided. Finally, acoustical field measurements of actual sound propagation from the operating array will be taken at the onset of the survey season. Should these measurements prove that associated sound energy is traveling farther than estimated, the safety zone will be adjusted accordingly and take estimates will be recalculated.

3.0 GRAY WHALES

Although the PGS IHA considers gray whales to be an extralimital species, at the request of the National Marine Fisheries Service (NMFS), the following evaluation has been completed for incorporation into the IHA application dated May 2008.

3.1 A Description of the Status, Distribution, and Seasonal Distribution (When Applicable) of the Affected Species or Stocks of Marine Mammals Likely to be Affected by Such Activities

The eastern Pacific or California gray whale population, like all large whale populations, was once hunted to near extinction, but has since recovered significantly from commercial whaling, and now numbers about 19,000 (revised Angliss and Outlaw 2005). The Pacific gray whale ranges from the Bering, Chukchi, and Beaufort Seas (in summer) to the Gulf of California (in winter) (Rice 1998); however, gray whales have also been documented foraging in waters off of Southeast Alaska, British Columbia,

Washington, Oregon, and California (Rice and Wolman 1971; Berzin 1984; Darling 1984; Quan 2000; Calambokidis et al. 2002). Most of the eastern north Pacific population makes a round-trip annual migration of more than 8,000 km (4,320 nm) from Alaska waters to Baja California in Mexico. From late May to early October, the majority of the population concentrates in the northern and western Bering Sea and the Chukchi Sea.

Typically, gray whales are found in shallow water, and usually remain closer to shore than any other large cetacean. Gray whales are considered common summer residents in the nearshore waters of the eastern Chukchi Sea, and occasionally are seen in the Beaufort Sea east of Point Barrow in late summer, as far east as Smith Bay (Green et al. 2007). On wintering grounds, mainly along the west coast of Baja California, gray whales habitat shallow, nearly land-locked lagoons and bays (Rice et al. 1981). From late February to June, the population migrates back to arctic and subarctic seas (Rice and Wolman 1971). Angliss and Outlaw (2005) recently estimated the Pacific gray whale population at about 19,000 based on surveys conducted in central California in 2000/2001 and 2001/2002, and suggested that the population may have declined from earlier estimates possibly due to the populations reaching carrying capacity. The eastern Pacific stock was removed from the Endangered Species List in 1994 and is not considered by NMFS to be a strategic stock.

3.2 Anticipated Impact of the Activity on the Species or Stock

Gray whales in the immediate area of seismic activity will likely show some behavioral changes. The changes in behavior, however, depend upon distance from the seismic source and are expected to be minimal. In a study including gray whales, behavioral responses were observed when the whales were subjected to seismic sounds between 160 and 170 dB re 1µPa. Studies in the Bering Sea by Malme et al (1986, 1988) showed the responses of gray whales to seismic sound pulses from a 100 cu in airgun array. Fifty percent of feeding whales stopped feeding when exposed to sound levels of 173 dB re 1µPa on average, and 10 percent stopped feeding at a received sound level of 163 dB re 1µPa. One whale study found indications of behavioral changes such as increased swim speed and shorter blow periods for seismic activities at a distance of up to 30 km (Würsig et al. 1999). However, when conducting shore-based counts Johnson (2007) did not mention any change in behavior and found no significance between abundance and seismic activity.

Data on short-term reactions (or lack of reactions) of cetaceans to impulsive noises do not necessarily provide information about long-term effects. It is not known whether impulsive noises affect reproductive rate or distribution and habitat use in subsequent days or years. Gray whales continued to migrate annually along the west coast of North America despite intermittent seismic exploration (and much ship traffic) in that area for decades (Malme et al. 1984; Richardson et al. 1995; Angliss and Outlaw 2005).

3.3 By Age, Sex, and Reproductive Condition (if Possible) the Number of Marine Mammals (by Species) that May be Taken by Each Type of Taking Identified in Paragraph (a)(5) of this Section, and the Number of Times Such Takings by Each Type of Taking Are Likely to Occur

PGS does not expect to encounter gray whales in the seismic survey area. There are currently no reliable abundance or density estimates for gray whales in the Beaufort Sea, but the number of individual whales is acknowledged to be very low and very few sightings have ever been recorded as far east as the Project Area. Although there are essentially no recent records of gray whales occurring in the project vicinity, recent reports (e.g., Green et al. 2007) suggest gray whales may be penetrating deeper into the Beaufort

Sea, thus, a slight chance does exist for sightings of gray whales. For this reason a take estimate for 2 (individual or as mother/calf pair) gray whales is requested.

4.0 REFERENCES

Angliss, R.P. and R. Outlaw. 2005. *Draft Marine Mammal Stock Assessment Reports (SARS) by Species/Stock*. Revised July 2005. NMFS. AFSC Center. Seattle, WA. 229 p. Available online at: http://www.nmfs.noaa.gov/pr/readingrm/MMSARS/draft05alaskareportall.pdf

Berzin, A. A. 1984. *Soviet studies on the distribution and numbers of the gray whale in the Bering and Chukchi Seas from 1968 to 1982.* Pp. 409-419, In M. L. Jones, S. L. Swartz, and S. Leatherwood (eds.), The Gray Whale (*Eschrichtius robustus)*. Academic Press, Inc., Orlando. xxiv + 600 pp.

Calambokidis, J., J. D. Darling, V. Deeke, P. Gearin, M. Gosho, W. Megill, C. M. Tombach, D. Goley, C.Toropova and B. Gisbourne. 2002. *Abundance, range and movements of a feeding aggregation of gray whales* (Eschrichtius robustus) *from California and southeastern Alaska in 1998*. Journal of Cetacean Research and Management. 4(3):267- 276.

Darling, J. D. 1984. *Gray whales off Vancouver Island, British Columbia*. Pp. 267-287; *In* M. L. Jones, S.L. Swartz, and S. Leatherwood (eds.), The Gray Whale, *Eschrichtius robustus*. Academic Press, Inc., Orlando. xxiv + 600 pp.

Green, G.A., K. Hashagen, D. Lee. 2007. *Marine Mammal Monitoring Program; FEX Barging Project,2007*. Unpublished Report to FEX, L.P., Anchorage, Alaska, from Tetra Tech EC, Bothell, Washington.

Johnson S.R., W.J. Richardson, S.B.Yazvenko, S.A. Blokin, G. Gailey, M.R. Jenkerson, S.K. Meier, H.R. Melton, M.W. Newcomer, A.S. Perlov, S.A Ruetenko, B. Würsig, C.R. Martin, and D.E. Egging. 2007. *A western gray whale mitigation and monitoring program for a 3-D seismic survey, Sakhalin Island, Russia*. Environmental Monitoring and Assessment. 134:1-19

Malme, C.I., P.R. Miles, C.W. Clark, P. Tyack, and J.E. Bird. 1984. *Investigations of the potential effects of underwater noise from petroleum industry activities on migrating gray whale behavior/Phase II: January 1984 migration.* BBN Rep. 5586. Rep. from Bolt Beranek & Newman Inc., Cambridge, MA, for U.S. Minerals Manage. Serv., Anchorage, AK. NTIS PB86-218377.

Malme, C.I., B. Würsig, J.E. Bird, and P. Tyack. 1986. *Behavioral responses of gray whales to industrial noise: feeding observations and predictive modeling.* Outer Cont. Shelf Environ. Assess. Progr., Final Rep. Princ. Invest., NOAA, Anchorage, AK 56(1988):393-600. BBN Rep. 6265. 600 p. OCS Study MMS 88-0048; NTIS PB88-249008.

Malme, C.I., B. Würsig, J.E. Bird, and P. Tyack. 1988. *Observations of feeding gray whale responses to controlled industrial noise exposure*. p. 55-73 *In*: W.M. Sackinger, M.O. Jeffries, J.L. Imm and S.D. Treacy (eds.), Port and ocean engineering under arctic conditions, vol. II. Geophysical Inst., Univ. Alaska, Fairbanks, AK. 111 p.

Quan, J. 2000. *Summer resident gray whales of Washington State: Policy, biological and management implications of Makah whaling*. M.S. Thesis. School of Marine Affairs, University of Washington. Seattle, WA.

Rice, D.W. 1998. *Marine mammals of the world, systematics and distribution*. Special Publication 4. Society of Marine Mammalogy, Allen Press, Lawrence, KS. 231 p.

Rice, D.W. and A.A. Wolman. 1971. *The life history and ecology of the gray whale (Eschrichtius robustus)*. American Society of Mammalogy Special Publication 3. 142 p.

Rice, D. W., A. A. Wolman, D. E. Withrow, and L. A. Fleischer. 1981. *Gray whales on the winter grounds in Baja California.* Report International Whaling Commission. 31:477-493.

Würsig, B.G., D.W. Weller, A.M. Burdin, S.H. Reeve, A.L Bradford, S.A. Blokhin and R.L Brownell (Jr.). 1999. *Gray whales summering off Sakhalin Island, Far East Russia: July-October 1997.* A joint U.S.-Russian scientific investigation. Final Report by Texas A&M Univ., College Station, TX, and Kamchatka Inst. Ecol. and Nature Manage., Russian Acad. Sci., Kamchatka, Russia, for Sakhalin Energy Investment Co. Ltd and Exxon Neftegaz Ltd, Yuzhno-Sakhalinsk, Russia. 101 p.

Array plot with profiles annotated

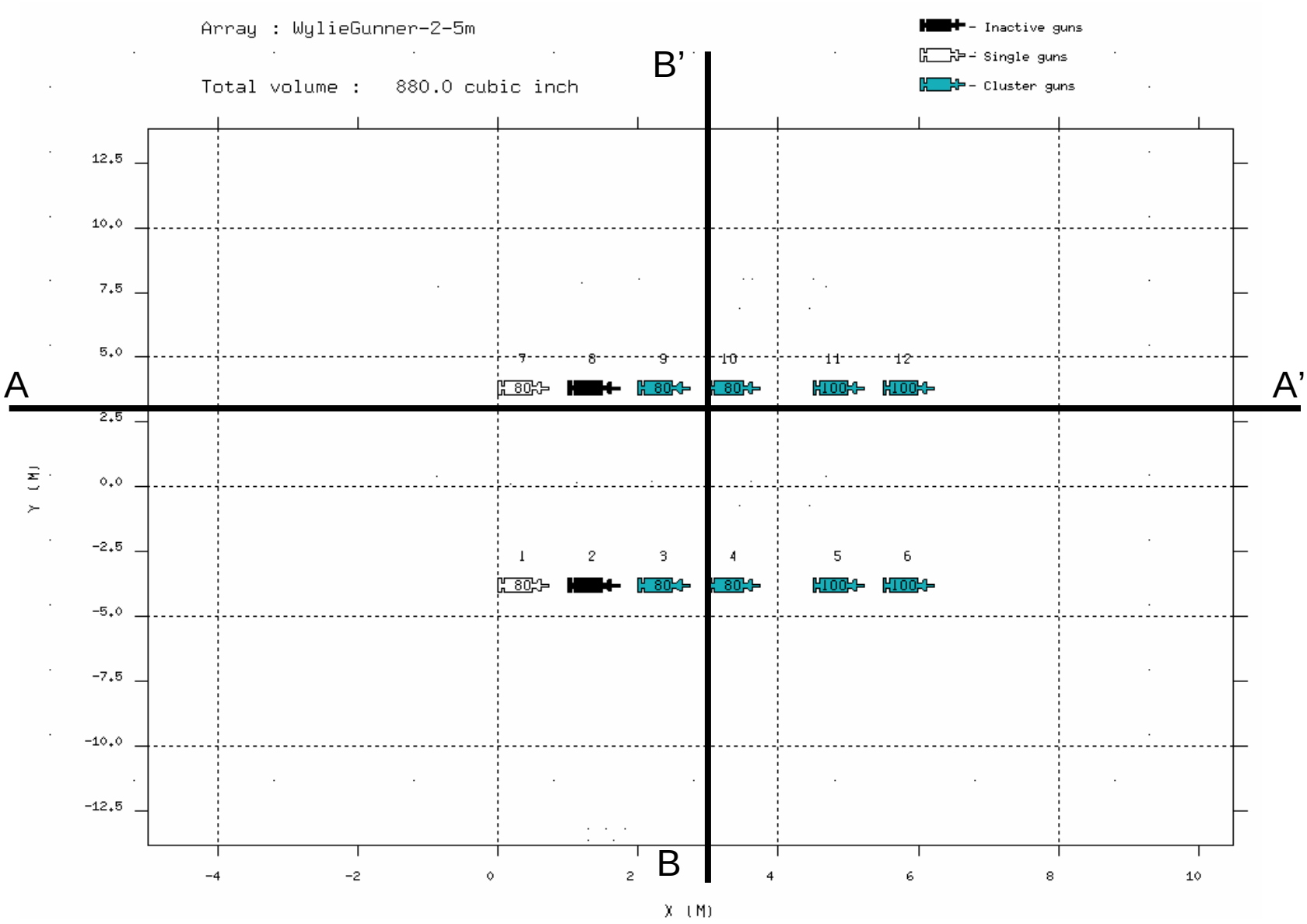

880ci array at 2.5m

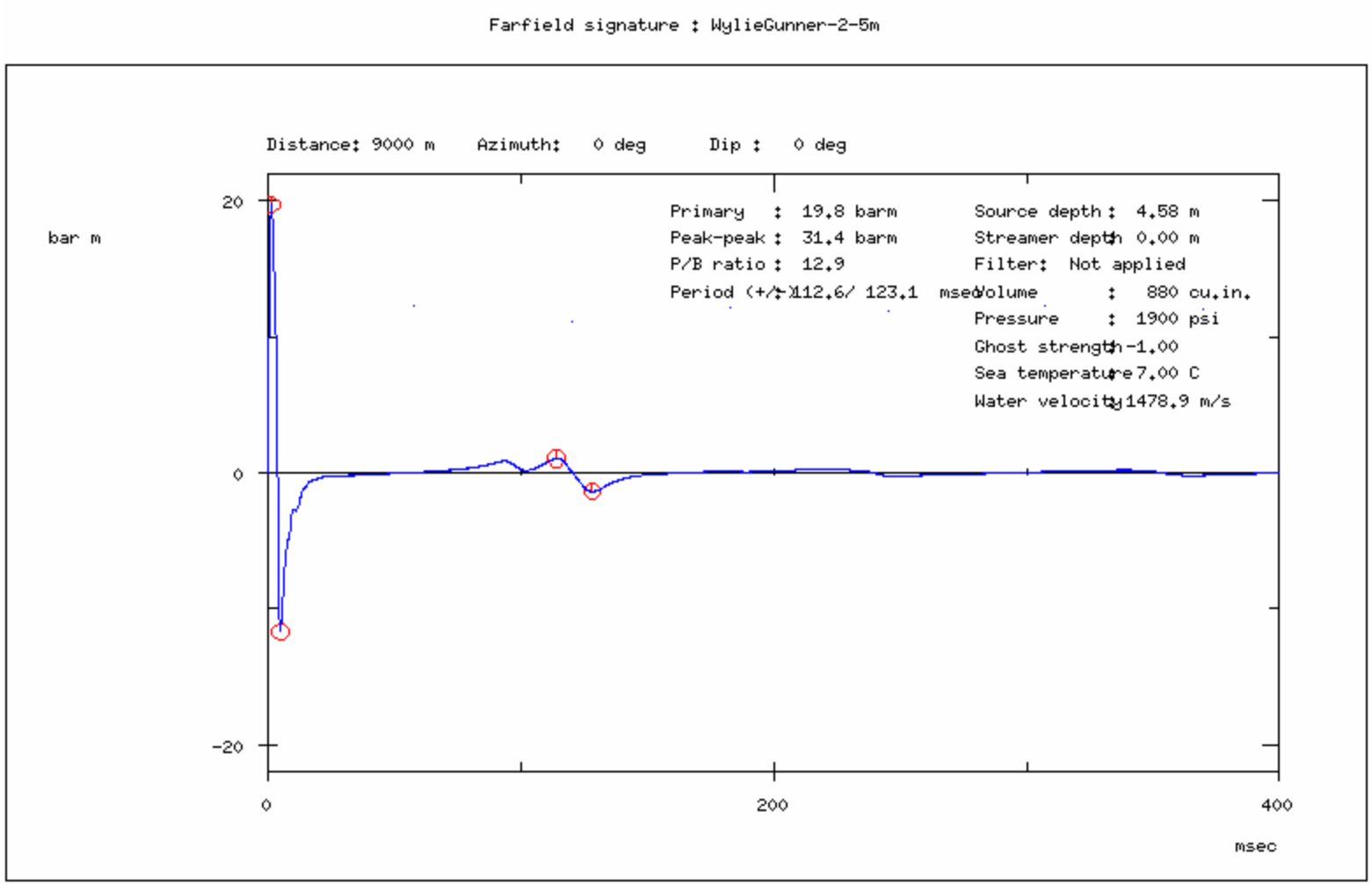

880ci array at 2.5m

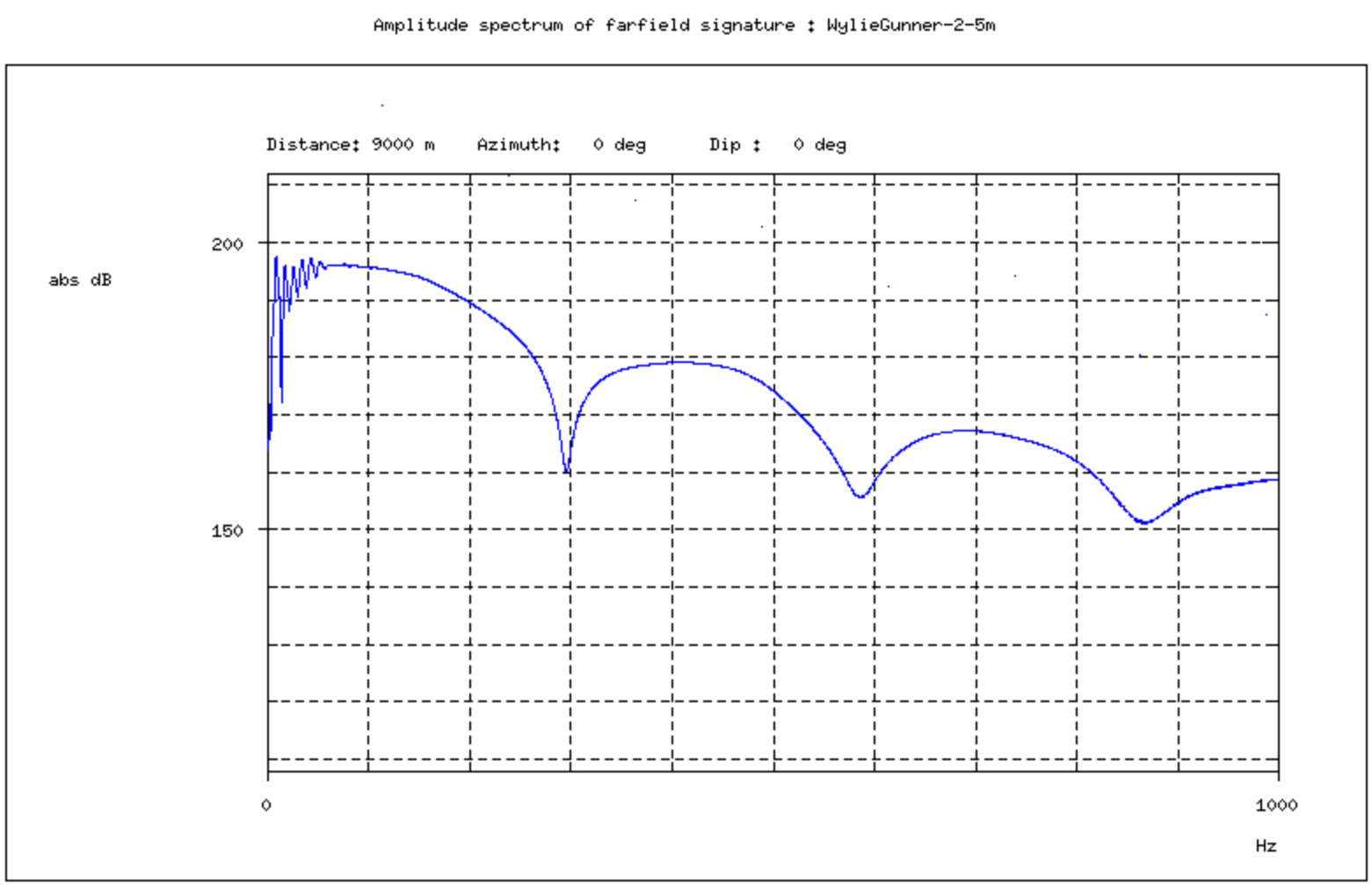

Inline Maximum Amplitude Profile (A-A’)

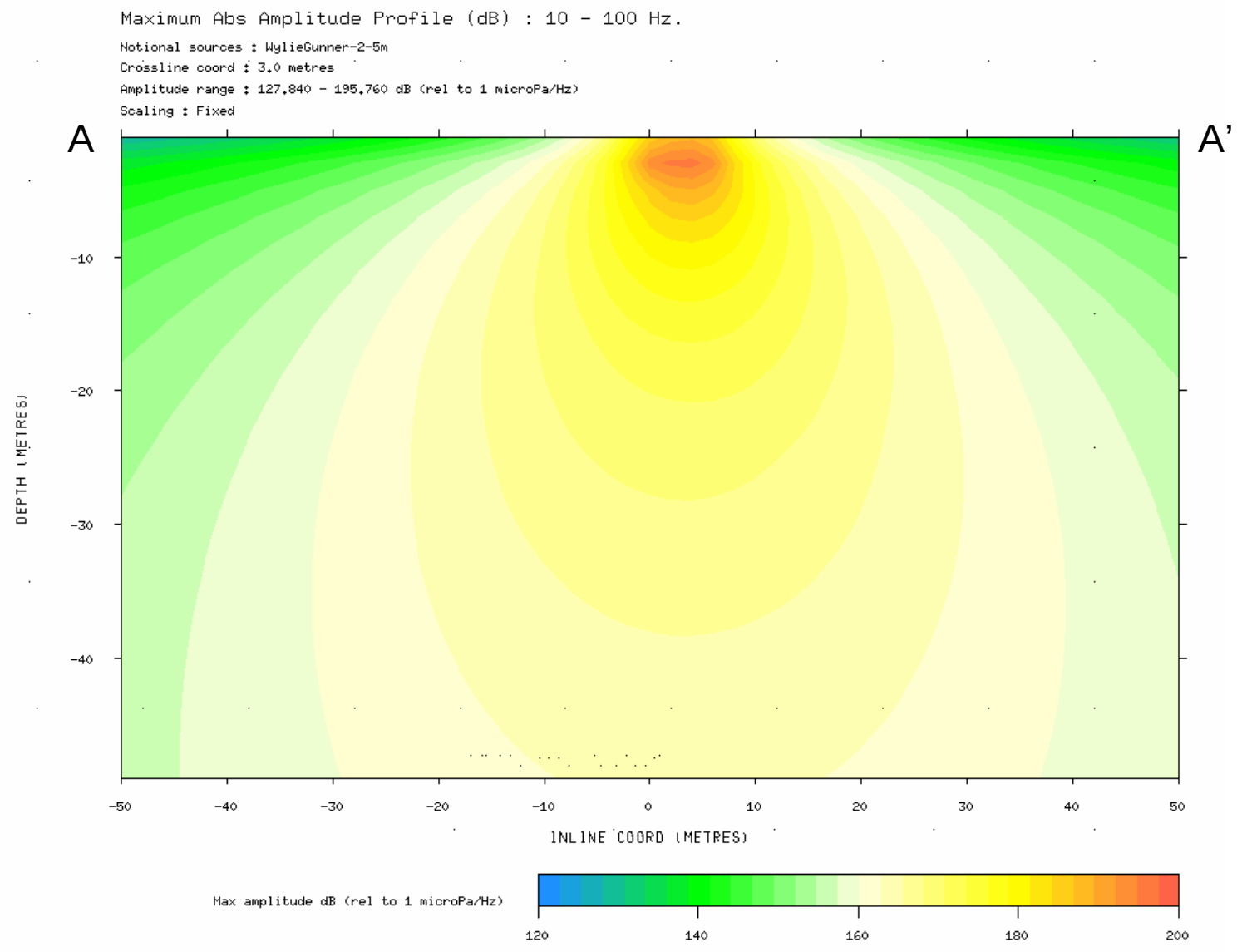

Crossline Maximum Amplitude Profile (B-B’)

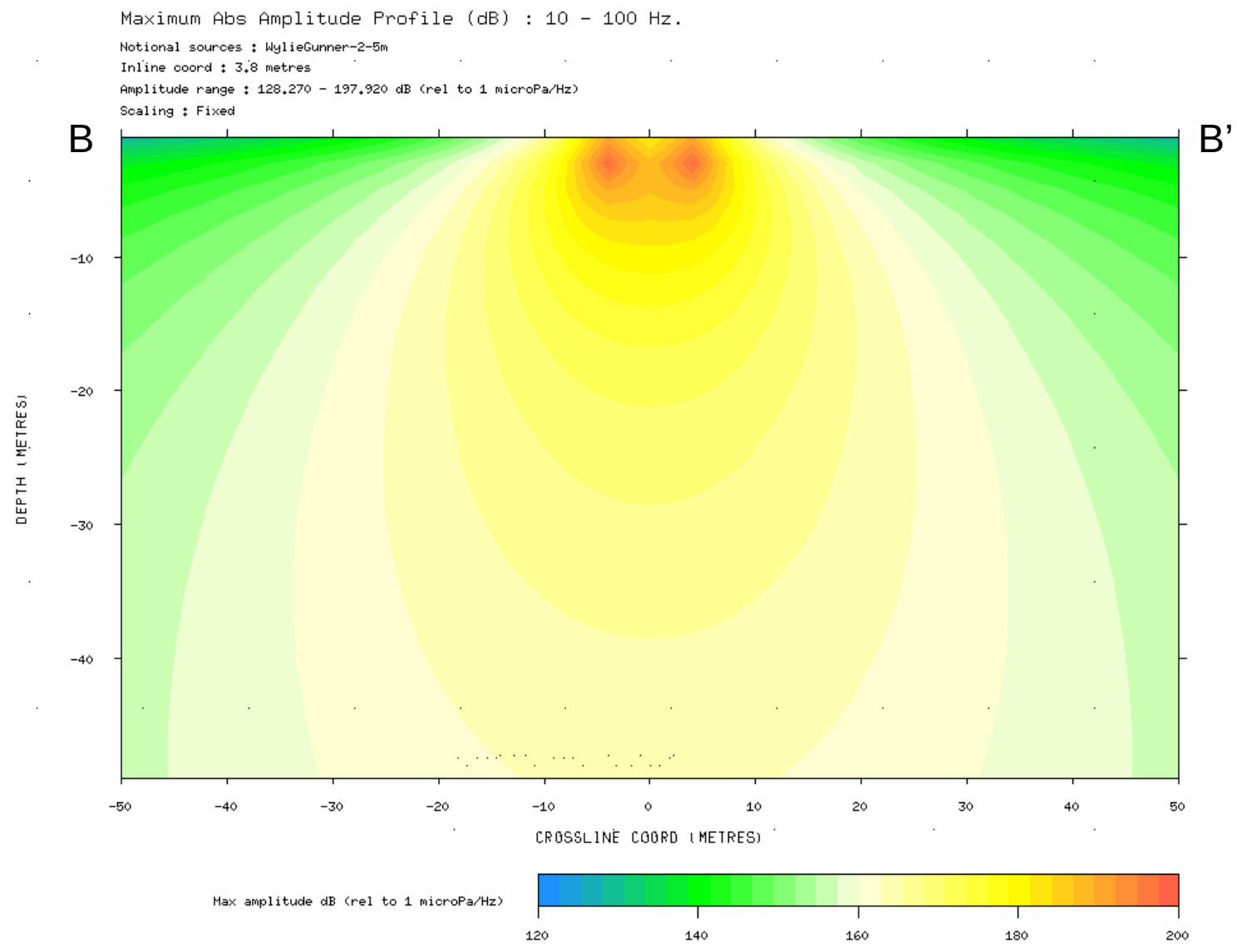

**THIS PAGE
INTENTIONALLY
LEFT BLANK**

Appendix A
The QCD Modeling Scheme

The QCD modeling scheme.

by

Rune Mittet

Sting Research
Rosenborg gt. 17
N-7014 Trondheim, Norway

Date : September 16, 2005

Contents

1 INTRODUCTION

The purpose of this document is to describe the modeling schemes implemented in the QCD code. How to start the QCD modeling schemes and technical issues are discussed in the user guide, manual.ps .

The QCD code is implemented to handle several modeling problems at an optimum speed of calculation. The simplest case is 2D acoustic modeling with constant density. More advanced modes are 3D visco-elastic modeling with variable density and elastic plane layer (cylinder symmetric) modeling with absorption and anisotropy.

Coarse-grid methods like pseudo-spectral methods (Fornberg, 1975; Kosloff and Baysal, 1982) or high order finite-difference methods (Holberg, 1987) are ideally suited for implementing fast and memory efficient 2-D or 3-D elastic modeling schemes (Edwards et al., 1985; Mittet et al., 1988; Reshef et al., 1988).

The errors related to these schemes can be separated into four classes:

* Errors due to approximations of temporal and spatial derivatives.

* Undesired reflections from the edges of the model.

* Representation of internal surfaces and free surfaces.

* Source and receiver positions for coarse grids.

The errors due to approximations of temporal and spatial derivatives can be neglected if the pseudo-spectral method is used in conjunction with the Rapid Expansion Method (Tal-Ezer, 1986, Tal-Ezer et al., 1987). However, if a finer sampling of the model is desirable (more than 3 nodes per shortest wavelength), then the finite-difference method becomes appealing since it is numerically more efficient than the pseudo-spectral method. The errors due to spatial differentiations can be made arbitrary small by using optimized operators (Holberg, 1987). The operator length can be chosen depending on the required number of nodes per shortest wavelength.

The undesired reflections from the edges of the model can be reduced either by transparent boundary conditions (Clayton and Enquist, 1977) or by absorbing boundary conditions (Cerjan et al., 1985) or by combining these two types of boundary conditions. The problem is still not completely solved. Waves impinging on the edges of the model generate some backscattered noise for all practical implementations of these methods. Using the Rapid Expansion Method for time integration seems to increase these difficulties.

Representation of internal interfaces is still a problem. As pointed out by Fornberg (1988), the roughness in the discretization of a smooth interface not aligned with the grid acts as a source of noise. Fornberg (1988) proposed to solve the problem of implementing an arbitrary interface by a mapping method. Some properties of these types of errors were discussed in Mittet and Buland (1994). Mittet and Renlie (1996) showed how direct averaging

of medium properties corresponded to introducing a false layer. A method for averaging medium properties given by Chang and Randall (1988), Randall et al. (1991), remove this unwanted false layer. In this report a simple implementation of the elastic free surface for staggered grid modeling schemes is given. This problem was treated by Levander (1988) using an image method. Tessmer et al. (1994) gave a solution to the problem by a boundary method based on characteristics. Several implementations of the elastic free surface were studied in Robertsson et al. (1995). The scheme presented here do neither require additional nodes above the free surface nor the isolation of characteristic modes near the free surface. An accurate free surface boundary condition is obtained at the nodes on the edges of the model by a modification of density and Lamé parameters on these nodes and by boundary conditions on the time variant fields. Thus, the same numerical algorithm us used internally and on the edges of the model.

2 CONTINUOUS FORMULATION

Viscoelastic wave propagation is governed by the equations of motion and the constitutive relations.

Let $a_i(\boldsymbol{x},t)$ denote a component of the particle acceleration vector, and $\sigma_{ij}(\boldsymbol{x},t)$ a component of the stress tensor. The particle acceleration components $a_i(\boldsymbol{x},t)$ are related to the stress components through the equations of motion,

$$\begin{aligned} a_x(\boldsymbol{x},t) &= \rho^{-1}(\boldsymbol{x})\left[\partial_x\sigma_{xx}(\boldsymbol{x},t)+\partial_y\sigma_{xy}(\boldsymbol{x},t)+\partial_z\sigma_{xz}(\boldsymbol{x},t)+f_x(\boldsymbol{x},t)\right], \\ a_y(\boldsymbol{x},t) &= \rho^{-1}(\boldsymbol{x})\left[\partial_x\sigma_{xy}(\boldsymbol{x},t)+\partial_y\sigma_{yy}(\boldsymbol{x},t)+\partial_z\sigma_{yz}(\boldsymbol{x},t)+f_y(\boldsymbol{x},t)\right], \\ a_z(\boldsymbol{x},t) &= \rho^{-1}(\boldsymbol{x})\left[\partial_x\sigma_{xz}(\boldsymbol{x},t)+\partial_y\sigma_{yz}(\boldsymbol{x},t)+\partial_z\sigma_{zz}(\boldsymbol{x},t)+f_z(\boldsymbol{x},t)\right], \end{aligned} \tag{1}$$

where $\rho(\boldsymbol{x})$ is the density and $f_i(\boldsymbol{x},t)$ is a force density which represent the source term. The spatial properties of $f_i(\boldsymbol{x},t)$ determine if the source behaves as an airgun or a seismic vibrator or any other source type. In the frequency domain, attenuation is modeled by replacing the real Hooke's tensor with a complex Hooke's tensor. In the time domain, however, attenuation turns the constitutive relation into a convolutional integral which is not suitable for finite-difference modeling schemes. To overcome this problem, the absorption is modeled by a set of viscoelastic relaxation mechanisms (Emmerich and Korn 1987; Carcione et al., 1988). The complications with the convolutional integral are then reduced to solving an additional set of first-order differential equations for a set of stress-memory functions. With this type of Generalized Maxwell body, causality is always secured and any type of linear absorption mechanism can be represented by adding relaxation mechanisms. The elastic constitutive relations including attenuation are given in Mittet and Renlie, (1996) as,

$$\sigma_{ij}(\boldsymbol{x},t) = \int_{-\infty}^{t} c_{ijkl}(\boldsymbol{x},t-\tau)\varepsilon_{kl}(\boldsymbol{x},\tau)d\tau, \tag{2}$$

in the convolutional form. Here $c_{ijkl}(\boldsymbol{x},t)$ is a component of the time dependent Hooke's tensor and $\varepsilon_{kl}(\boldsymbol{x},\tau)$ is a component of the strain tensor. With a derivation similar to Emmerich and Korn, 1987, equation (2) can be transformed to,

$$\sigma_{ij}(\boldsymbol{x},t) = c^U_{ijkl}(\boldsymbol{x})\varepsilon_{kl}(\boldsymbol{x},t) - \sum_{s=1}^{M} \gamma^s_{ij}(\boldsymbol{x},t), \tag{3}$$

where the stress-memory functions $\gamma^s_{ij}(\boldsymbol{x},t)$ satisfy,

$$\partial_t \gamma^s_{ij}(\boldsymbol{x},t) + \omega^s(\boldsymbol{x})\gamma^s_{ij}(\boldsymbol{x},t) = \omega^s(\boldsymbol{x})\Delta c^s_{ijkl}(\boldsymbol{x})\varepsilon_{kl}(\boldsymbol{x},t). \tag{4}$$

Here, M is the number of relaxation mechanisms, the $\omega^s(\boldsymbol{x})$'s are relaxation angular frequencies. These are resonance frequencies, such that the attenuation will have peaks at these frequencies. The relaxed or low frequency limit of the Hooke's tensor is $c^R_{ijkl}(\boldsymbol{x})$ and the unrelaxed or high frequency limit is $c^U_{ijkl}(\boldsymbol{x})$ and,

$$\Delta c^s_{ijkl}(\boldsymbol{x}) = c^U_{ijkl}(\boldsymbol{x}) - c^R_{ijkl}(\boldsymbol{x}). \tag{5}$$

In the present implementation we use one attenuation mechanism for the P-waves and one attenuation mechanism for the S-waves. The resonance frequency is assumed to be identical for both mechanisms and independent of spatial location. With a proper choice of $\omega^s = \omega_0$, the attenuation is very close to constant Q in the seismic band, but still causal.

The constitutive relation for isotropic 3-D wave propagation including attenuation is,

$$\begin{aligned}
\partial_t^2\sigma_{xx}(\boldsymbol{x},t) &= \lambda^U(\boldsymbol{x})\left[\partial_x a_x(\boldsymbol{x},t) + \partial_y a_y(\boldsymbol{x},t) + \partial_z a_z(\boldsymbol{x},t)\right] \\
&+ 2\mu^U(\boldsymbol{x})\left[\partial_x a_x(\boldsymbol{x},t)\right] - \eta^P_{xx}(\boldsymbol{x},t) - \eta^S_{xx}(\boldsymbol{x},t), \\
\partial_t^2\sigma_{yy}(\boldsymbol{x},t) &= \lambda^U(\boldsymbol{x})\left[\partial_x a_x(\boldsymbol{x},t) + \partial_y a_y(\boldsymbol{x},t) + \partial_z a_z(\boldsymbol{x},t)\right] \\
&+ 2\mu^U(\boldsymbol{x})\left[\partial_y a_y(\boldsymbol{x},t)\right] - \eta^P_{yy}(\boldsymbol{x},t) - \eta^S_{yy}(\boldsymbol{x},t), \\
\partial_t^2\sigma_{zz}(\boldsymbol{x},t) &= \lambda^U(\boldsymbol{x})\left[\partial_x a_x(\boldsymbol{x},t) + \partial_y a_y(\boldsymbol{x},t) + \partial_z a_z(\boldsymbol{x},t)\right] \\
&+ 2\mu^U(\boldsymbol{x})\left[\partial_z a_z(\boldsymbol{x},t)\right] - \eta^P_{zz}(\boldsymbol{x},t) - \eta^S_{zz}(\boldsymbol{x},t), \\
\partial_t^2\sigma_{xy}(\boldsymbol{x},t) &= \mu^U(\boldsymbol{x})\left[\partial_x a_y(\boldsymbol{x},t) + \partial_y a_x(\boldsymbol{x},t)\right] - \eta^P_{xy}(\boldsymbol{x},t) - \eta^S_{xy}(\boldsymbol{x},t), \\
\partial_t^2\sigma_{xz}(\boldsymbol{x},t) &= \mu^U(\boldsymbol{x})\left[\partial_x a_z(\boldsymbol{x},t) + \partial_z a_x(\boldsymbol{x},t)\right] - \eta^P_{xz}(\boldsymbol{x},t) - \eta^S_{xz}(\boldsymbol{x},t), \\
\partial_t^2\sigma_{yz}(\boldsymbol{x},t) &= \mu^U(\boldsymbol{x})\left[\partial_y a_z(\boldsymbol{x},t) + \partial_z a_y(\boldsymbol{x},t)\right] - \eta^P_{yz}(\boldsymbol{x},t) - \eta^S_{yz}(\boldsymbol{x},t),
\end{aligned} \tag{6}$$

where $\lambda^U(\boldsymbol{x})$ and $\mu^U(\boldsymbol{x})$ are the unrelaxed Lamé parameters. Using,

$$\partial_t^2\gamma^s_{ij}(\boldsymbol{x},t) = \eta^s_{ij}(\boldsymbol{x},t), \tag{7}$$

and assuming that we have either a P-wave attenuation mechanism $s = P$ or and S-wave attenuation mechanism $s = S$ the additional equations to solve can be expressed as

$$\begin{aligned}
\partial_t \eta^P_{xx}(\boldsymbol{x},t) &+ \omega_0 \eta^P_{xx}(\boldsymbol{x},t) = \omega_0 \Delta\lambda^P(\boldsymbol{x}) \left[\partial_x a_x(\boldsymbol{x},t) + \partial_y a_y(\boldsymbol{x},t) + \partial_z a_z(\boldsymbol{x},t)\right], \\
\partial_t \eta^P_{yy}(\boldsymbol{x},t) &+ \omega_0 \eta^P_{yy}(\boldsymbol{x},t) = \omega_0 \Delta\lambda^P(\boldsymbol{x}) \left[\partial_x a_x(\boldsymbol{x},t) + \partial_y a_y(\boldsymbol{x},t) + \partial_z a_z(\boldsymbol{x},t)\right], \\
\partial_t \eta^P_{zz}(\boldsymbol{x},t) &+ \omega_0 \eta^P_{zz}(\boldsymbol{x},t) = \omega_0 \Delta\lambda^P(\boldsymbol{x}) \left[\partial_x a_x(\boldsymbol{x},t) + \partial_y a_y(\boldsymbol{x},t) + \partial_z a_z(\boldsymbol{x},t)\right], \\
\partial_t \eta^P_{xy}(\boldsymbol{x},t) &= 0, \\
\partial_t \eta^P_{xz}(\boldsymbol{x},t) &= 0, \\
\partial_t \eta^P_{yz}(\boldsymbol{x},t) &= 0,
\end{aligned} \tag{8}$$

and

$$\begin{aligned}
\partial_t \eta^S_{xx}(\boldsymbol{x},t) &+ \omega_0 \eta^S_{xx}(\boldsymbol{x},t) = -2\omega_0 \Delta\mu^S(\boldsymbol{x}) \left[\partial_y a_y(\boldsymbol{x},t) + \partial_z a_z(\boldsymbol{x},t)\right], \\
\partial_t \eta^S_{yy}(\boldsymbol{x},t) &+ \omega_0 \eta^S_{yy}(\boldsymbol{x},t) = -2\omega_0 \Delta\mu^S(\boldsymbol{x}) \left[\partial_x a_x(\boldsymbol{x},t) + \partial_z a_z(\boldsymbol{x},t)\right], \\
\partial_t \eta^S_{zz}(\boldsymbol{x},t) &+ \omega_0 \eta^S_{zz}(\boldsymbol{x},t) = -2\omega_0 \Delta\mu^S(\boldsymbol{x}) \left[\partial_x a_x(\boldsymbol{x},t) + \partial_y a_y(\boldsymbol{x},t)\right], \\
\partial_t \eta^S_{xy}(\boldsymbol{x},t) &+ \omega_0 \eta^S_{xy}(\boldsymbol{x},t) = \omega_0 \Delta\mu^S(\boldsymbol{x}) \left[\partial_x a_y(\boldsymbol{x},t) + \partial_y a_x(\boldsymbol{x},t)\right], \\
\partial_t \eta^S_{xz}(\boldsymbol{x},t) &+ \omega_0 \eta^S_{xz}(\boldsymbol{x},t) = \omega_0 \Delta\mu^S(\boldsymbol{x}) \left[\partial_x a_z(\boldsymbol{x},t) + \partial_z a_x(\boldsymbol{x},t)\right], \\
\partial_t \eta^S_{yz}(\boldsymbol{x},t) &+ \omega_0 \eta^S_{yz}(\boldsymbol{x},t) = \omega_0 \Delta\mu^S(\boldsymbol{x}) \left[\partial_y a_z(\boldsymbol{x},t) + \partial_z a_y(\boldsymbol{x},t)\right].
\end{aligned} \tag{9}$$

The relations between the $Q^P(\boldsymbol{x})$ and $Q^S(\boldsymbol{x})$ models and the Lamé parameters can be found by the frequency domain relations given at the resonance frequency $\omega = \omega_0$,

$$\begin{aligned}
\Delta\lambda^P(\boldsymbol{x}) &= \frac{2\lambda^R(\boldsymbol{x})}{(Q^P(\boldsymbol{x}) - 1)}, \\
\Delta\mu^P(\boldsymbol{x}) &= 0, \\
\Delta\lambda^S(\boldsymbol{x}) &= \frac{-4\mu^R(\boldsymbol{x})}{(Q^S(\boldsymbol{x}) - 1)}, \\
\Delta\mu^S(\boldsymbol{x}) &= \frac{2\mu^R(\boldsymbol{x})}{(Q^S(\boldsymbol{x}) - 1)}.
\end{aligned} \tag{10}$$

The relaxed Lamé parameters are given by the low frequency limits of the P-wave and the S-wave velocities

$$\begin{aligned}
\lambda^R(\boldsymbol{x}) &= \rho(\boldsymbol{x}) \left[v_P^2(\boldsymbol{x}) - 2v_S^2(\boldsymbol{x})\right], \\
\mu^R(\boldsymbol{x}) &= \rho(\boldsymbol{x}) v_S^2(\boldsymbol{x}).
\end{aligned} \tag{11}$$

3 TI MEDIUM

The constitutive relation for a TI or hexagonal symmetric medium is,

$$\begin{aligned}
\sigma_{xx}(\boldsymbol{x},t) &= c_{xxxx}(\boldsymbol{x})\varepsilon_{xx}(\boldsymbol{x},t) + c_{xxyy}(\boldsymbol{x})\varepsilon_{yy}(\boldsymbol{x},t) + c_{xxzz}(\boldsymbol{x})\varepsilon_{zz}(\boldsymbol{x},t),\\
\sigma_{yy}(\boldsymbol{x},t) &= c_{yyxx}(\boldsymbol{x})\varepsilon_{xx}(\boldsymbol{x},t) + c_{yyyy}(\boldsymbol{x})\varepsilon_{yy}(\boldsymbol{x},t) + c_{yyzz}(\boldsymbol{x})\varepsilon_{zz}(\boldsymbol{x},t),\\
\sigma_{zz}(\boldsymbol{x},t) &= c_{zzxx}(\boldsymbol{x})\varepsilon_{xx}(\boldsymbol{x},t) + c_{zzyy}(\boldsymbol{x})\varepsilon_{yy}(\boldsymbol{x},t) + c_{zzzz}(\boldsymbol{x})\varepsilon_{zz}(\boldsymbol{x},t),\\
\sigma_{xy}(\boldsymbol{x},t) &= c_{xyxy}(\boldsymbol{x})\varepsilon_{xy}(\boldsymbol{x},t),\\
\sigma_{xz}(\boldsymbol{x},t) &= c_{xzxz}(\boldsymbol{x})\varepsilon_{xz}(\boldsymbol{x},t),\\
\sigma_{yz}(\boldsymbol{x},t) &= c_{yzyz}(\boldsymbol{x})\varepsilon_{yz}(\boldsymbol{x},t).
\end{aligned} \tag{12}$$

A much used notation is,

$$\begin{aligned}
A(\boldsymbol{x}) &= c_{xxxx}(\boldsymbol{x}) = c_{yyyy}(\boldsymbol{x}),\\
B(\boldsymbol{x}) &= c_{xxyy}(\boldsymbol{x}) = c_{yyxx}(\boldsymbol{x}),\\
C(\boldsymbol{x}) &= c_{zzzz}(\boldsymbol{x}),\\
F(\boldsymbol{x}) &= c_{xxzz}(\boldsymbol{x}) = c_{yyzz}(\boldsymbol{x}) = c_{zzxx}(\boldsymbol{x}) = c_{zzyy}(\boldsymbol{x})\\
2N(\boldsymbol{x}) &= c_{xyxy}(\boldsymbol{x}),\\
2L(\boldsymbol{x}) &= c_{xzxz}(\boldsymbol{x}) = c_{yzyz}(\boldsymbol{x}).
\end{aligned} \tag{13}$$

with $A(\boldsymbol{x}) = B(\boldsymbol{x}) + 2N(\boldsymbol{x})$, which give 5 independent parameters for TI media. In the isotropic limit we have

$$\begin{aligned}
B(\boldsymbol{x}) &= \lambda(\boldsymbol{x}),\\
C(\boldsymbol{x}) &= \lambda(\boldsymbol{x}) + 2\mu(\boldsymbol{x}),\\
F(\boldsymbol{x}) &= \lambda(\boldsymbol{x}),\\
N(\boldsymbol{x}) &= \mu(\boldsymbol{x}),\\
L(\boldsymbol{x}) &= \mu(\boldsymbol{x}).
\end{aligned} \tag{14}$$

Using Thompson parameters $\epsilon(\boldsymbol{x})$, $\delta(\boldsymbol{x})$ and $\gamma(\boldsymbol{x})$, we can also write,

$$\begin{aligned}
L(\boldsymbol{x}) &= \mu_1(\boldsymbol{x}) = \rho v_S^2(\boldsymbol{x}),\\
C(\boldsymbol{x}) &= \lambda_1(\boldsymbol{x}) + 2\mu_1(\boldsymbol{x}) = \rho v_P^2(\boldsymbol{x}),\\
N(\boldsymbol{x}) &= \mu_2(\boldsymbol{x}) = \mu_1(\boldsymbol{x})(1 + 2\gamma(\boldsymbol{x})),\\
B(\boldsymbol{x}) &= \lambda_2(\boldsymbol{x}) = \lambda_1(\boldsymbol{x})(1 + 2\epsilon(\boldsymbol{x})) + 4\mu_1(\boldsymbol{x})(\epsilon(\boldsymbol{x}) - \gamma(\boldsymbol{x})),\\
F(\boldsymbol{x}) &= \lambda_3(\boldsymbol{x}) = (\lambda_1(\boldsymbol{x}) + \mu_1(\boldsymbol{x}))\sqrt{1 + 2\delta(\boldsymbol{x})\frac{\lambda_1(\boldsymbol{x}) + 2\mu_1(\boldsymbol{x})}{\lambda_1(\boldsymbol{x}) + \mu_1(\boldsymbol{x})}} - \mu_1(\boldsymbol{x})
\end{aligned} \tag{15}$$

where $v_P(\boldsymbol{x})$ and $v_S(\boldsymbol{x})$ are the vertical P-wave and S-wave velocities respectively.

The constitutive relations can be expressed,

$$\begin{aligned}
\partial_t^2\sigma_{xx}(\boldsymbol{x},t) &= (\lambda_2(\boldsymbol{x})+2\mu_2(\boldsymbol{x}))\partial_x a_x(\boldsymbol{x},t)+\lambda_2(\boldsymbol{x})\partial_y a_y(\boldsymbol{x},t)+\lambda_3(\boldsymbol{x})\partial_z a_z(\boldsymbol{x},t),\\
\partial_t^2\sigma_{yy}(\boldsymbol{x},t) &= \lambda_2(\boldsymbol{x})\partial_x a_x(\boldsymbol{x},t)+(\lambda_2(\boldsymbol{x})+2\mu_2(\boldsymbol{x}))\partial_y a_y(\boldsymbol{x},t)+\lambda_3(\boldsymbol{x})\partial_z a_z(\boldsymbol{x},t),\\
\partial_t^2\sigma_{zz}(\boldsymbol{x},t) &= \lambda_3(\boldsymbol{x})\partial_x a_x(\boldsymbol{x},t)+\lambda_3(\boldsymbol{x})\partial_y a_y(\boldsymbol{x},t)+(\lambda_1(\boldsymbol{x})+2\mu_1(\boldsymbol{x}))\partial_z a_z(\boldsymbol{x},t),\\
\partial_t^2\sigma_{xy}(\boldsymbol{x},t) &= \mu_2(\boldsymbol{x})\left[\partial_x a_y(\boldsymbol{x},t)+\partial_y a_x(\boldsymbol{x},t)\right],\\
\partial_t^2\sigma_{xz}(\boldsymbol{x},t) &= \mu_1(\boldsymbol{x})\left[\partial_x a_z(\boldsymbol{x},t)+\partial_z a_x(\boldsymbol{x},t)\right],\\
\partial_t^2\sigma_{yz}(\boldsymbol{x},t) &= \mu_1(\boldsymbol{x})\left[\partial_y a_z(\boldsymbol{x},t)+\partial_z a_y(\boldsymbol{x},t)\right].
\end{aligned} \tag{16}$$

Absorption is included using equations (3), (4) and (5). Having only one P-wave and one S-wave Q-factor available, we use,

$$\begin{aligned}
\Delta\lambda_1^P(\boldsymbol{x}) &= \frac{2\lambda_1^R(\boldsymbol{x})}{(Q^P(\boldsymbol{x})-1)},\\
\Delta\lambda_2^P(\boldsymbol{x}) &= \frac{2\lambda_2^R(\boldsymbol{x})}{(Q^P(\boldsymbol{x})-1)},\\
\Delta\lambda_3^P(\boldsymbol{x}) &= \frac{2\lambda_3^R(\boldsymbol{x})}{(Q^P(\boldsymbol{x})-1)},\\
\Delta\mu_1^P(\boldsymbol{x}) &= 0,\\
\Delta\mu_2^P(\boldsymbol{x}) &= 0,\\
\Delta\lambda_1^S(\boldsymbol{x}) &= \frac{-4\mu_1^R(\boldsymbol{x})}{(Q^S(\boldsymbol{x})-1)},\\
\Delta\lambda_2^S(\boldsymbol{x}) &= \frac{-4\mu_2^R(\boldsymbol{x})}{(Q^S(\boldsymbol{x})-1)},\\
\Delta\lambda_3^S(\boldsymbol{x}) &= \frac{-4\mu_2^R(\boldsymbol{x})}{(Q^S(\boldsymbol{x})-1)},\\
\Delta\mu_1^S(\boldsymbol{x}) &= \frac{2\mu_1^R(\boldsymbol{x})}{(Q^S(\boldsymbol{x})-1)},\\
\Delta\mu_2^S(\boldsymbol{x}) &= \frac{2\mu_2^R(\boldsymbol{x})}{(Q^S(\boldsymbol{x})-1)}.
\end{aligned} \tag{17}$$

Thus, both horizontal and vertical waves have the same Q-factors.

4 CYLINDER SYMMETRIC MODELING

For cylinder symmetric modeling, only source elements with spherical symmetry are included. These are notional source signatures and forces in the z direction. However, the lateral

translational invariance of the model is used to treat realistic source arrays. The methodology is different from the 2D and 3D schemes. The exciting sources are bandlimited Dirac delta distributions in both space and time. The resulting Green's tensors are spherically symmetric, but they are synthesized to give the response of an arbitrary source array. The resulting response function (pressure or particle velocities) need not be spherically symmetric.

The equation of motion for a cylinder symmetric medium with spherically symmetric source elements are,

$$\begin{aligned} a_r(\mathrm{r,z},t) &= \rho^{-1}(z)\left[\partial_r\sigma_{rr}(\mathrm{r,z},t) + \frac{\sigma_{rr}(\mathrm{r,z},t) - \sigma_{\theta\theta}(\mathrm{r,z},t)}{r} + \partial_z\sigma_{rz}(\mathrm{r,z},t) + f_r(\mathrm{r,z},t)\right], \\ a_\theta(\mathrm{r,z},t) &= 0, \\ a_z(\mathrm{r,z},t) &= \rho^{-1}(z)\left[\partial_r\sigma_{rz}(\mathrm{r,z},t) + \frac{\sigma_{rz}(\mathrm{r,z},t)}{r} + \partial_z\sigma_{zz}(\mathrm{r,z},t) + f_z(\mathrm{r,z},t)\right], \end{aligned} \tag{18}$$

and the constitutive relations are,

$$\begin{aligned} \partial_t^2\sigma_{rr}(\mathrm{r,z},t) &= (\lambda_2(z)+2\mu_2(z))\partial_r a_r(\mathrm{r,z},t) + \lambda_2(z)\frac{a_r(\mathrm{r,z},t)}{r} + \lambda_3(z)\partial_z a_z(\mathrm{r,z},t), \\ \partial_t^2\sigma_{\theta\theta}(\mathrm{r,z},t) &= \lambda_2(z)\partial_r a_r(\mathrm{r,z},t) + (\lambda_2(z)+2\mu_2(z))\frac{a_r(\mathrm{r,z},t)}{r} + \lambda_3(z)\partial_z a_z(\mathrm{r,z},t), \\ \partial_t^2\sigma_{zz}(\mathrm{r,z},t) &= \lambda_3(z)\partial_r a_r(\mathrm{r,z},t) + \lambda_3(z)\frac{a_r(\mathrm{r,z},t)}{r} + (\lambda_1(z)+2\mu_1(z))\partial_z a_z(\mathrm{r,z},t), \\ \partial_t^2\sigma_{r\theta}(\mathrm{r,z},t) &= 0, \\ \partial_t^2\sigma_{rz}(\mathrm{r,z},t) &= \mu_1(z)\left[\partial_r a_z(\mathrm{r,z},t) + \partial_z a_r(\mathrm{r,z},t)\right], \\ \partial_t^2\sigma_{\theta z}(\mathrm{r,z},t) &= 0. \end{aligned} \tag{19}$$

with the equations for absorption following a similar scheme.

5 DISCRETE FORMULATION

For simplicity I discuss the discrete formulation for a 2D scheme, the 3D and cylinder symmetric formulations are straight forward generalizations. The algorithm used here is an optimized high-order staggered-grid scheme, thus the terms forward and backward derivative operators are used. The optimized operator coefficients α_l are identical for both operators, but the output location differs. Let $\phi(i)$ be a discrete representation of the continuous field $\phi(x_k)$, where $x_k = (i-1)\Delta x_k$. Here Δx_k is the step length in the k-direction and x_k represents one of the spatial coordinates x, y or z. The forward and backward derivative operators in the k-direction, ∂_k^+ and ∂_k^-, (Holberg,1987) with operator halflength L, are given as,

$$\partial_k^+\phi(i) = \partial_k\phi(i+\tfrac{1}{2}) = \frac{1}{\Delta x_k}\sum_{l=1}^{L}\alpha_l\left[\phi(i+l) - \phi(i-(l-1))\right],$$

$$\partial_k^- \phi(i) \quad = \quad \partial_k \phi(i - \tfrac{1}{2}) = \frac{1}{\Delta x_k} \sum_{l=1}^{L} \alpha_l \left[\phi(i + (l-1)) - \phi(i-l) \right]. \tag{20}$$

The operator coefficients α_l are optimized, based on an error criterion for the group velocity. These operators are special cases of the more general operators discussed in appendix A. The operator halflength L can be varied in the QCD scheme. For $L = 1$ we have a typical low order scheme, where the required number of gridpoints per shortest wavelength G is of order 25 to 30, however, for $L = 8$ we have $G = 2.5$ which is close to the pseudo-spectral limit of $G = 2$. This give a very flexible scheme, where a low order algorithm can be used for fine sampling of the medium and a high order algorithm can be used for coarse sampling of the medium.

When implementing the wave equation in the QCD scheme, the source terms are moved from the equation of motion to the equation for the constitutive relations. This is a formal procedure which makes it easier to include notional source signatures in the calculation and the scheme is also easier to adapt to prestack elastic reverse time migration. The source tensor is in the following denoted $T_{ij}(\boldsymbol{x}, t)$

Let $\sigma_{mn}(\boldsymbol{x}, t) = \sigma_{mn}(x, z, t) = \sigma_{mn}((i-1)\Delta x, (j-1)\Delta z, t) = \sigma_{mn}(i, j, t)$ and likewise for the spatial discretization of all other quantities. The steplengths in x- and z-directions are Δx and Δz respectively.

Equation (1) implemented on a staggered grid can then be expressed,

$$\begin{aligned} a_x(i+\tfrac{1}{2}, j, t) &= \rho^{-1}(i+\tfrac{1}{2}, j) \left[\partial_x^+ \sigma_{xx}(i, j, t) + \partial_z^- \sigma_{xz}(i+\tfrac{1}{2}, j+\tfrac{1}{2}, t) \right], \\ a_z(i, j+\tfrac{1}{2}, t) &= \rho^{-1}(i, j+\tfrac{1}{2}) \left[\partial_z^+ \sigma_{zz}(i, j, t) + \partial_x^- \sigma_{xz}(i+\tfrac{1}{2}, j+\tfrac{1}{2}, t) \right]. \end{aligned} \tag{21}$$

The equations for the stress tensor is,

$$\begin{aligned} \partial_t^2 \sigma_{xx}(i, j, t) &= \lambda(i, j) \left[\partial_x^- a_x(i+\tfrac{1}{2}, j, t) + \partial_z^- a_z(i, j+\tfrac{1}{2}, t) \right] \\ &+ 2\mu(i, j) \left[\partial_x^- a_x(i+\tfrac{1}{2}, j, t) \right] - \eta_{xx}^P(i, j, t) - \eta_{xx}^S(i, j, t) + T_{xx}(i, j, t), \\ \partial_t^2 \sigma_{zz}(i, j, t) &= \lambda(i, j) \left[\partial_x^- a_x(i+\tfrac{1}{2}, j, t) + \partial_z^- a_z(i, j+\tfrac{1}{2}, t) \right] \\ &+ 2\mu(i, j) \left[\partial_z^- a_z(i, j+\tfrac{1}{2}, t) \right] - \eta_{zz}^P(i, j, t) - \eta_{zz}^S(i, j, t) + T_{zz}(i, j, t), \\ \partial_t^2 \sigma_{xz}(i+\tfrac{1}{2}, j+\tfrac{1}{2}, t) &= \mu(i+\tfrac{1}{2}, j+\tfrac{1}{2}) \left[\partial_x^+ a_z(i, j+\tfrac{1}{2}, t) + \partial_z^+ a_x(i+\tfrac{1}{2}, j, t) \right] \\ &- \eta_{xz}^P(i+\tfrac{1}{2}, j+\tfrac{1}{2}, t) - \eta_{xz}^S(i+\tfrac{1}{2}, j+\tfrac{1}{2}, t) + T_{xz}(i+\tfrac{1}{2}, j+\tfrac{1}{2}, t). \end{aligned} \tag{22}$$

The additional equations to solve are spatially discretized in the same way as above,

$$\begin{aligned} \partial_t \eta_{xx}^P(i, j, t) &+ \omega_0 \eta_{xx}^P(i, j, t) = \omega_0 \Delta\lambda^P(i, j) \left[\partial_x^- a_x(i+\tfrac{1}{2}, j, t) + \partial_z^- a_z(i, j+\tfrac{1}{2}, t) \right], \\ \partial_t \eta_{zz}^P(i, j, t) &+ \omega_0 \eta_{zz}^P(i, j, t) = \omega_0 \Delta\lambda^P(i, j) \left[\partial_x^- a_x(i+\tfrac{1}{2}, j, t) + \partial_z^- a_z(i, j+\tfrac{1}{2}, t) \right], \\ \partial_t \eta_{xz}^P(i+\tfrac{1}{2}, j+\tfrac{1}{2}, t) &= 0, \end{aligned} \tag{23}$$

and

$$\begin{aligned}
\partial_t \eta^S_{xx}(i,j,t) &+ \omega_0 \eta^S_{xx}(i,j,t) = -2\omega_0 \Delta\mu^S(i,j)\partial_z^- a_z(i,j+\tfrac{1}{2},t), \\
\partial_t \eta^S_{zz}(i,j,t) &+ \omega_0 \eta^S_{zz}(i,j,t) = -2\omega_0 \Delta\mu^S(i,j)\partial_x^- a_x(i+\tfrac{1}{2},j,t), \\
\partial_t \eta^S_{xz}(i+\tfrac{1}{2},j+\tfrac{1}{2},t) &+ \omega_0 \eta^S_{xz}(i+\tfrac{1}{2},j+\tfrac{1}{2},t) = \omega_0 \Delta\mu^S(i+\tfrac{1}{2},j+\tfrac{1}{2}) \\
&\quad \left[\partial_x^+ a_z(i,j+\tfrac{1}{2},t) + \partial_z^+ a_x(i+\tfrac{1}{2},j,t)\right].
\end{aligned} \tag{24}$$

In this scheme σ_{xx}, σ_{zz}, η_{xx}, η_{zz} can be said to be located on the reference grid, a_x is staggered half a node distance in the x-direction relative to the reference grid, a_z is staggered half a node distance in the z-direction relative to the reference grid and σ_{xz} and η_{xz} is staggered half a node distance in both the x-direction and the z-direction relative to the reference grid. The source tensor is also staggered in the same way.

The physical parameters are precalculated and given at the nodes where they are needed. This implies that two representations of the same inverse density model must be given, one shifted half a gridpoint in the x-direction relative to the reference grid, and one shifted half a gridpoint in the z-direction relative to the reference grid. That is,

$$\begin{aligned}
\rho^{-1}(i+\tfrac{1}{2},j) &= \frac{2}{\rho(i,j)+\rho(i+1,j)}, \\
\rho^{-1}(i,j+\tfrac{1}{2}) &= \frac{2}{\rho(i,j)+\rho(i,j+1)}.
\end{aligned} \tag{25}$$

The Lamé parameters λ and μ are needed on the reference grid but μ are also needed on the shifted grid. The scheme given by Chang and Randall (1988) is used. Thus with,

$$\begin{aligned}
\Xi(i+\tfrac{1}{2},j+\tfrac{1}{2}) &= 4\mu(i,j)\mu(i+1,j)\mu(i,j+1)\mu(i+1,j+1), \\
\Upsilon(i+\tfrac{1}{2},j+\tfrac{1}{2}) &= \mu(i,j)\mu(i+1,j)\mu(i,j+1) \\
&+ \mu(i,j)\mu(i+1,j)\mu(i+1,j+1) \\
&+ \mu(i,j)\mu(i,j+1)\mu(i+1,j+1) \\
&+ \mu(i+1,j)\mu(i,j+1)\mu(i+1,j+1),
\end{aligned} \tag{26}$$

the Lamé parameter μ on the σ_{xz} grid is,

$$\mu(i+\tfrac{1}{2},j+\tfrac{1}{2}) = \frac{\Xi(i+\tfrac{1}{2},j+\tfrac{1}{2})}{\Upsilon(i+\tfrac{1}{2},j+\tfrac{1}{2})}. \tag{27}$$

The difference between the unrelaxed and relaxed Lamé parameter μ, $\Delta\mu^S(i+\frac{1}{2},j+\frac{1}{2})$ is calculated in the same manner.

The time integration can be performed to a given order as described by Dablain, (1986), or by spectral methods (Tal-Ezer, 1986, Tal-Ezer et al., 1987). Here we give the equations for a second order time integration scheme. Let $t = n\Delta t$, where Δt is the temporal sampling interval. The following modeling scheme is based on finding the stress tensor at time $t+\Delta t = (n+1)\Delta t$ given that the stress tensor is known at times $t = n\Delta t$ and $t - \Delta t = (n-1)\Delta t$.

The first step is to calculate the particle accelerations,

$$\begin{aligned} a_x(i+\tfrac{1}{2},j,n) &= \rho^{-1}(i+\tfrac{1}{2},j)\left[\partial_x^+\sigma_{xx}(i,j,n) + \partial_z^-\sigma_{xz}(i+\tfrac{1}{2},j+\tfrac{1}{2},n)\right], \\ a_z(i,j+\tfrac{1}{2},n) &= \rho^{-1}(i,j+\tfrac{1}{2})\left[\partial_z^+\sigma_{zz}(i,j,n) + \partial_x^-\sigma_{xz}(i+\tfrac{1}{2},j+\tfrac{1}{2},n)\right]. \end{aligned} \tag{28}$$

The next step is to get the stress memory functions η_{ij} with the correct temporal staggering. Before the first timestep the following quantities are calculated,

$$\kappa = \frac{2-\omega_0\Delta t}{2+\omega_0\Delta t}, \tag{29}$$

and

$$\begin{aligned} \nu_1^P(i,j) &= \frac{2\omega_0\Delta t\Delta\lambda^P(i,j)}{2+\omega_0\Delta t}, \\ \nu_1^S(i,j) &= \frac{-4\omega_0\Delta t\Delta\mu^S(i,j)}{2+\omega_0\Delta t}, \\ \nu_2^S(i+\tfrac{1}{2},j+\tfrac{1}{2}) &= \frac{2\omega_0\Delta t\Delta\mu^S(i+\tfrac{1}{2},j+\tfrac{1}{2})}{2+\omega_0\Delta t}. \end{aligned} \tag{30}$$

Equation (23) is written,

$$\begin{aligned} \eta_{xx}^P(i,j,n+\tfrac{1}{2}) &= \eta_{xx}^P(i,j,n-\tfrac{1}{2}) + \nu_1^P(i,j)\left[\partial_x^- a_x(i+\tfrac{1}{2},j,n) + \partial_z^- a_z(i,j+\tfrac{1}{2},n)\right], \\ \eta_{zz}^P(i,j,n+\tfrac{1}{2}) &= \eta_{xx}^P(i,j,n+\tfrac{1}{2}), \\ \partial_t\eta_{xz}^P(i+\tfrac{1}{2},j+\tfrac{1}{2},n) &= 0, \end{aligned} \tag{31}$$

and equation (24) is written,

$$\begin{aligned} \eta_{xx}^S(i,j,n+\tfrac{1}{2}) &= \eta_{xx}^S(i,j,n-\tfrac{1}{2}) + \nu_1^S(i,j)\partial_z^- a_z(i,j+\tfrac{1}{2},n), \\ \eta_{zz}^S(i,j,n+\tfrac{1}{2}) &= \eta_{zz}^S(i,j,n-\tfrac{1}{2}) + \nu_1^S(i,j)\partial_x^- a_x(i+\tfrac{1}{2},j,n), \\ \eta_{xz}^S(i+\tfrac{1}{2},j+\tfrac{1}{2},n+\tfrac{1}{2}) &= \eta_{xz}^S(i+\tfrac{1}{2},j+\tfrac{1}{2},n-\tfrac{1}{2}) \\ &+ \nu_2^S(i+\tfrac{1}{2},j+\tfrac{1}{2})\left[\partial_x^+ a_z(i,j+\tfrac{1}{2},n) + \partial_z^+ a_x(i+\tfrac{1}{2},j,n)\right]. \end{aligned} \tag{32}$$

The stress components can now be updated. The term Δt^2 arising from the second order time derivative is included in the Lamé parameters,

$$\begin{aligned}
\sigma_{xx}(i,j,n+1) &= 2\sigma_{xx}(i,j,n) - \sigma_{xx}(i,j,n-1) \\
&+ \lambda(i,j)\left[\partial_x^- a_x(i+\tfrac{1}{2},j,n) + \partial_z^- a_z(i,j+\tfrac{1}{2},n)\right] \\
&+ 2\mu(i,j)\left[\partial_x^- a_x(i+\tfrac{1}{2},j,n)\right] \\
&- \tfrac{1}{2}\left[\eta_{xx}^P(i,j,n-\tfrac{1}{2}) + \eta_{xx}^P(i,j,n+\tfrac{1}{2})\right] \\
&- \tfrac{1}{2}\left[\eta_{xx}^S(i,j,n-\tfrac{1}{2}) + \eta_{xx}^S(i,j,n+\tfrac{1}{2})\right] \\
&+ T_{xx}(i,j,n), \\
\sigma_{zz}(i,j,n+1) &= 2\sigma_{zz}(i,j,n) - \sigma_{zz}(i,j,n-1) \\
&+ \lambda(i,j)\left[\partial_x^- a_x(i+\tfrac{1}{2},j,n) + \partial_z^- a_z(i,j+\tfrac{1}{2},n)\right] \\
&+ 2\mu(i,j)\left[\partial_z^- a_z(i+\tfrac{1}{2},j,n)\right] \\
&- \tfrac{1}{2}\left[\eta_{zz}^P(i,j,n-\tfrac{1}{2}) + \eta_{zz}^P(i,j,n+\tfrac{1}{2})\right] \\
&- \tfrac{1}{2}\left[\eta_{zz}^S(i,j,n-\tfrac{1}{2}) + \eta_{zz}^S(i,j,n+\tfrac{1}{2})\right] \\
&+ T_{zz}(i,j,n), \\
\sigma_{xz}(i+\tfrac{1}{2},j+\tfrac{1}{2},n+1) &= 2\sigma_{xz}(i+\tfrac{1}{2},j+\tfrac{1}{2},n) - \sigma_{xz}(i+\tfrac{1}{2},j+\tfrac{1}{2},n-1) \\
&+ \mu(i+\tfrac{1}{2},j+\tfrac{1}{2})\left[\partial_x^+ a_z(i,j+\tfrac{1}{2},n) + \partial_z^+ a_x(i+\tfrac{1}{2},j,n)\right] \\
&- \tfrac{1}{2}\left[\eta_{xz}^P(i+\tfrac{1}{2},j+\tfrac{1}{2},n-\tfrac{1}{2}) + \eta_{xz}^P(i+\tfrac{1}{2},j+\tfrac{1}{2},n+\tfrac{1}{2})\right] \\
&- \tfrac{1}{2}\left[\eta_{xz}^S(i+\tfrac{1}{2},j+\tfrac{1}{2},n-\tfrac{1}{2}) + \eta_{xz}^S(i+\tfrac{1}{2},j+\tfrac{1}{2},n+\tfrac{1}{2})\right] \\
&+ T_{xz}(i+\tfrac{1}{2},j+\tfrac{1}{2},n).
\end{aligned} \tag{33}$$

6 FREE SURFACE

The free surface is assumed to be horizontal and at depth $z = 0$. The dynamic boundary conditions for the elastic free surface requires that the normal component of the traction is zero, that is,

$$\begin{aligned}
\sigma_{xz}(x,0,t) &= 0, \\
\sigma_{zz}(x,0,t) &= 0.
\end{aligned} \tag{34}$$

Combining equation (6) with equation (34) the last stress component on the free surface is given by,

$$\partial_t^2 \sigma_{xx}(x,0,t) = \frac{4\mu(x,0)\left[\lambda(x,0)+\mu(x,0)\right]}{\lambda(x,0)+2\mu(x,0)} \partial_x a_x(x,0,t). \tag{35}$$

In the present implementation the elastic free surface is located on the first node in depth (that is for all i with j=1). The stress and particle acceleration components in the staggered grid scheme, given at these nodes, are σ_{xx}, σ_{zz} and a_x. All field components and medium parameters are assumed to be zero above the free surface. The σ_{zz} component is zero on the free surface. The partial differential equations to be solved for the fields on the free surface are,

$$a_x(i+\tfrac{1}{2},j,t) \quad = \quad \rho^{-1}(i+\tfrac{1}{2},j)\left[\partial_x^+ \sigma_{xx}(i,j,t) + \partial_z^- \sigma_{xz}(i+\tfrac{1}{2},j+\tfrac{1}{2},t)\right], \tag{36}$$

and

$$\partial_t^2 \sigma_{xx}(i,1,t) = \frac{4\mu(i,1)\left[\lambda(i,1)+\mu(i,1)\right]}{\lambda(i,1)+2\mu(i,1)} \partial_x^- a_x(i+\tfrac{1}{2},1,t). \tag{37}$$

The medium parameters, ρ, λ and μ, in these equations must be modified on the free surface to give a correct description of both the wave propagation on the elastic free surface and likewise of the reflections from the elastic free surface. It is assumed that the density on the free surface is given by an averaging of the vacuum value and the internal value. Thus,

$$a_x(i+\tfrac{1}{2},1,t) = \frac{4}{\rho(i,1)+\rho(i+1,1)}\left[\partial_x^+ \sigma_{xx}(i,j,t) + \partial_z^- \sigma_{xz}(i+\tfrac{1}{2},j+\tfrac{1}{2},t)\right]. \tag{38}$$

Assuming that also the Lamé parameters λ and μ behave as the density gives,

$$\partial_t^2 \sigma_{xx}(i,1,t) = \frac{\mu(i,1)\left[\lambda(i,1)+\mu(i,1)\right]}{\frac{1}{2}\lambda(i,1)+\mu(i,1)} \partial_x a_x(i+\tfrac{1}{2},j,t). \tag{39}$$

Testing and comparison with solutions calculated with frequency wavenumber modeling revealed that this is still not sufficient to obtain a proper elastic free surface boundary condition for the staggered finite difference scheme. However, if in addition the Lamé parameter λ is set to zero on the first node in depth, that is,

$$\lambda(i,1) \to 0,$$

then a good discrete approximation to the free surface is obtained. The last assumption is not justified theoretically, but can be justified by comparison with analytical methods or by comparison with the frequency wavenumber modeling scheme. Equation (39) takes the form,

$$\partial_t^2 \sigma_{xx}(i,1,t) = \mu(i,1)\partial_x a_x(i+\tfrac{1}{2},j,t). \tag{40}$$

which is equation (22) with $\lambda(i,1) \to 0$ and $\mu(i,1) \to \frac{1}{2}\mu(i,1)$.

The implementation of the proposed boundary condition is very simple. The equations (22) and (21) are solved for all nodes of the finite difference grid, including $j = 1$. The medium parameters on the free surface are, however, given special treatment,

$$\begin{aligned} \rho^{-1}(i+\tfrac{1}{2},1) &\to \frac{4}{\rho(i,1)+\rho(i+1,1)}, \\ \lambda(i,1) &\to 0, \\ \mu(i,1) &\to \frac{1}{2}\mu(i,1). \end{aligned} \tag{41}$$

In addition, for each timestep it is ensured that $\sigma_{zz}(i,1,t) = 0$.

7 SOURCES AND RECEIVERS

It is assumed that the source tensor $T_{ij}(\boldsymbol{x},t)$ can be separated into a spatial and a temporal term, that is,

$$T_{ij}(\boldsymbol{x},t) = D_i(\boldsymbol{x})g_j(t), \tag{42}$$

or

$$T_{ij}(\boldsymbol{x},t) = D_{ij}(\boldsymbol{x})g(t). \tag{43}$$

The spatial term is assumed to be a combination of monopole and dipole contributions. As an example of a directional force in the x-direction, $f_x(\boldsymbol{x},t) = \delta(\boldsymbol{x}-\boldsymbol{x}_s)g_x(t)$ we have, except for a scaling with the density at location $\boldsymbol{x}_s$,

$$\begin{aligned} T_{xx}(\boldsymbol{x},t) &= \partial_x\delta(x-x_s)\delta(z-z_s)g_x(t), \\ T_{xz}(\boldsymbol{x},t) &= 0.0, \\ T_{zx}(\boldsymbol{x},t) &= \delta(x-x_s)\partial_z\delta(z-z_s)g_x(t), \\ T_{zz}(\boldsymbol{x},t) &= 0.0. \end{aligned} \tag{44}$$

A notional source signature is as,

$$\begin{aligned} T_{xx}(\boldsymbol{x},t) &= \delta(x-x_s)\delta(z-z_s)g(t), \\ T_{xz}(\boldsymbol{x},t) &= 0.0, \\ T_{zx}(\boldsymbol{x},t) &= 0.0, \\ T_{zz}(\boldsymbol{x},t) &= \delta(x-x_s)\delta(z-z_s)g(t). \end{aligned} \tag{45}$$

The problem which has to be solved is to find high-order bandlimited Dirac delta function operators which also can handle the situations when $\boldsymbol{x}_s$ do not coincide with a grid node. This is of special importance for coarse grid schemes with steplengths of order 10 m.

The development of such operators is discussed in appendix A and appendix B. The operator table containing the derivative operator is α_l^η and the operator table containing the shift operator is β_l^η. The 2D Dirac delta function $\delta(x-x_s)\delta(z-z_s$ will be distributed over several nodes using the combined operator $\alpha_{l_x}^{\eta_x}\alpha_{l_z}^{\eta_z}$. The value of $\alpha_{l_x}^{\eta_x}\alpha_{l_z}^{\eta_z}$ for the case where the source coincide with a node position is $\frac{1}{\Delta x}\frac{1}{\Delta z}$ at the source node and zero otherwise. If the source do not coincide with a node the source timefunction is typically be distributed over 4-16 nodes in both the x- and z-direction.

The recording operator for a general recording position $\boldsymbol{x}_r$ is identical to the bandlimited Dirac delta function operator described in appendix B. Let

$$(x_r, z_r) = ((i-1)\Delta x + \eta_i \Delta x, (j-1)\Delta z + \eta_j \Delta x), \tag{46}$$

as can be seen from equation (B-3), if the operator table β_l^η is known, then an arbitrary receiver position in the model can be reached by the expression

$$a_x(x_r, z_r, n) = \sum_{l_i=-L_i}^{L_i} \sum_{l_j=-L_j}^{L_j} \beta_{l_i}^{\eta_i} \beta_{l_j}^{\eta_j} a_x(i+l_i, j+l_j, n). \tag{47}$$

using the x-component of the particle acceleration as an example here.

8 SOLVED AND UNSOLVED PROBLEMS

The described scheme has the following advantages. It will be very fast on both super-scalar and vector computers, when properly implemented for the given architecture. The scheme is very flexible and can be operated as a classical low- order scheme with dense sampling. It is however much more efficient to use coarser sampling and the scheme, using long derivative operators, can also operate close to the Nyquist limit. Thus, the scheme has nearly the same properties as a pseudo-spectral scheme in this limit. Scaling on multitasking computers is generally very good. The numerical dispersion is low and well controlled when proper derivative operators are chosen. The free surface is well described and behaves properly

when number of nodes per shortest wavelength (propagating waves) is above 5-6. For coarser sampling some dispersion may occur. The reason for this is that the Rayleigh wave actually varies faster in space than homogeneous waves for the same source maximum frequency and a finer grid is then required to avoid dispersion. With the introduction of the generalized source and receiver operators, sources and receivers can be placed with a precision of one hundredth of the node distance. This is an important improvement, especially for coarse grids. The internal interfaces including water/solid interfaces are properly described. Calibration tests using analytical solutions and fk-algorithms reveals that interfaces are located midway between node locations. Continuous fields like pressure and normal component of particle velocity can be recorded at arbitrary positions near the water/solid interface.

There are still some remaining problems with the present implementation of the scheme. Recording of the parallel component of particle velocity close to a water/solid interface ($v_x(\boldsymbol{x}, t)$ for a horizontal interface) can be performed only on node position. The reason is that this field component is discontinuous over the water/solid interface. A more complicated operator than the one described in Appendix B is required in order to use general receiver coordinates in this case.

Diffractions from dipping interfaces may result using coarse grids This is the well known staircase effect. It is most prominent in low velocity zones. A free surface with topography have the same problems. Both effects may be remedied with a mapping method as originally described by Fornberg (1988).

Very low velocity zones, as the low S-wave velocities usually encountered directly below the seafloor, requires very fine sampling and hence large CPU times. The present method requires the same sampling intervals for the whole model. This problem may also be solved with a mapping method somewhat different from the one proposed by Fornberg (1988).

Absorbing boundary conditions using the method of Cerjan et al. (1985) works well for medium and coarse grids. There are problems with this method for fine grids. The absorbing zones must cover many node positions. The method could probably be combined with a transparent boundary condition, giving reduced edge effects for all grid types. This is presently not implemented.

At present the scheme is second order in time. For most cases this seems to be sufficient as found by comparison with fk-results. There may, however, be cases where increased numerical precision from the time integration is required. This may be obtained by going to higher order schemes as described by Dablain (1986) or using Runge-Kutta methods. The second order scheme also makes it simpler to convert the present scheme to an elastic reverse time integration scheme.

References

[1] Carcione, J.M., Kosloff, D., and Kosloff, R., 1988, Viscoacoustic wave propagation simulation in the earth: Geophysics, **53**,769–777.

[2] Cerjan C., Kosloff, D., Kosloff, R., and Reshef, M., 1985, A nonreflecting boundary condition for discrete acoustic and elastic wave equations Geophysics, **50**,705–708.

[3] Chang, H. W., and Randall, C. J., 1988, Finite-difference time-domain modeling of elastic wave propagation in the cylindrical coordinate system, *in* Proc IEEE Ultrasonics Symp, 397–402.

[4] Clayton, R. W., and Enquist, B., 1977, Absorbing boundary conditions for acoustic and elastic wave equations bssa, **67**,1529–1540.

[5] Dablain, M. A., 1986, The application of high-order differencing to the scalar wave equation: Geophysics, **51**,54–66.

[6] Edwards, M., Hsiung, D., Kosloff, D., and Reshef, M., 1985, Elastic 3-D forward modeling by the fourier method, *in* 55th Ann. Internat. Mtg., Soc. Expl. Geophys., Expanded Abstracts.

[7] Emmerich, H., and Korn, M., 1987, Incorporation of attenuation into time-domain computations of seismic wavwfields: Geophysics, **52**,1252–1264.

[8] Fornberg, B., 1975, On a fourier method for the integration of hyperbolic equations: Soc.Ind.Appl.Math.,J.Numer.Anal., 509–528.

[9] Fornberg, B., 1988, The pseudospectral method: Accurate representation of interfaces in elastic wave calculations: Geophysics, 625–637.

[10] Holberg, O., 1987, Computational aspects of the choice of operator and sampling interval for numerical differentiation in large-scale simulation of wave phenomena: Geophys. Prosp., **37**,629–655.

[11] Kosloff, D.D., and Baysal, E., 1982, Forward modeling by a fourier method Geophysics, **47**,1402–1412.

[12] Levander A.R., 1988, Fourth-order finite-difference P-SV seismograms Geophysics, **53**,1425–1436.

[13] Mittet, R., and Buland, A., 1995, Numerical errors due to non-aligned interfaces in coarse-grid modeling schemes J. of Seismic Exploration, **4**,5–16.

[14] Mittet, R., Holberg, O., Arntsen, B., and Amundsen, L., 1988, Fast finite-difference modeling of 3-D elastic wave propagation, *in* 58th Ann. Internat. Mtg., Soc. Expl. Geophys., Expanded Abstracts, 1308–1311.

[15] Mittet, R., and Renlie, R., 1996, High-order finite-difference modeling of multipole logging in formations with anisotropic attenuation and elasticity Geophysics, **61**,21–33.

[16] Randall, C. J., Scheibner, D. J., and Wu, P. T., 1991, Multipole borehole acoustic waveforms: Synthetic logs with beds borehole washouts Geophysics, **56**,17578–1769.

[17] Reshef, M, Kosloff, D., Edwards, M., and Hsiung, C., 1988, Three-dimensional elastic modeling by the fourier method Geophysics, **53**,1184–1193.

[18] Robertsson J.O.A., Levander, A., Symes W.W., and Holliger, K., 1995, A comparative study of free-surface boundary conditions for finite-difference simulation of elastic/viscoelastic wave propagation, *in* 65nd SEG Annual Meetg. and Exhibition Expanded Abstracts, 1277–1280.

[19] Tal-Ezer, H., 1986, Spectral methods in time for hyperbolic equations Siam J. Numerical Anal., **23**,11–20.

[20] Tal-Ezer, H., Kosloff, D., and Koren, Z., 1987, An accurate scheme for seismic forward modelling Geophys. Prosp., **35**,479–490.

[21] Tessmer, E., and Kosloff D., 1994, 3-D elastic modeling with surface topography by a chebychev spectral method Geophysics, **59**,464–473.

Appendix A: Dipole and derivative operator.

The dipole operator needed in the source term of the wave equation or in the implementation of the boundary condition is the derivative of the Dirac delta function,

$$\partial_x \delta(x - x_s). \tag{A-1}$$

The derivative of the Dirac delta function also defines the convolutional derivative operator,

$$\begin{aligned} \partial_x \phi(x + \delta x) &= \int_{-\infty}^{\infty} dx' \{-\partial'_x \delta(x' - \delta x)\} \phi(x + x') \\ &= d_x^{\delta x} * \phi(x). \end{aligned} \tag{A-2}$$

Assume that this operator can be bandlimited and is to be used on a regularly sampled function with sampling interval Δx. Let $x = i\Delta x$ with i integer. Let $\delta x = \eta \Delta x$ with η a real number such that $-0.5 \leq \eta \leq 0.5$. The two special cases $\eta = -0.5$ and $\eta = 0.5$ will be the forward and backward derivative operators given by Holberg, (1987). The discretized version of $d_x^{\delta x}$ is denoted D_x^{η} and the bandlimited Dirac delta function is denoted $\tilde{\delta}$,

$$\begin{aligned} \partial_x \phi(j\Delta x + \eta \Delta x) &= D_x^{\eta} \phi(j\Delta x) \\ &= \sum_{l=-L}^{L} \Delta x [-\partial_x \tilde{\delta}(l\Delta x - \eta \Delta x)] \phi(j\Delta x + l\Delta x) \\ &= \sum_{l=-L}^{L} \alpha_l^{\eta} \phi_{j+l}. \end{aligned} \tag{A-3}$$

The Fourier response of D_x^{η} is,

$$D^{\eta}(k) = \frac{1}{\Delta x} \sum_{l=-L}^{L} \alpha_l^{\eta} e^{ik(l-\eta)\Delta x}. \tag{A-4}$$

Let the response $D^{\eta}(k)$ be represented by,

$$D^{\eta}(k) = ik(1 + \varepsilon^{\eta}(k)) \tag{A-5}$$

where $\varepsilon^{\eta}(k)$ is the relative error in frequency response of the operator D_x^{η}. The derivative of the frequency response of $D^{\eta}(k)$ is

$$\partial_k D^{\eta}(k) = i(1 + \varepsilon^{\eta}(k) + k\partial_k \varepsilon^{\eta}(k)). \tag{A-6}$$

If it is required that $D^{\eta}(k)$ should be as close to ik as possible then,

$$\min(D^{\eta}(k) - ik) = \min(\varepsilon^{\eta}(k)). \tag{A-7}$$

If it is required that the derivative of $D^\eta(k)$ with respect to k should be as close to i as possible then,

$$\min(\frac{1}{i}\partial_k(D^\eta(k)-1) = \min(\varepsilon^\eta(k) + k\partial_k\varepsilon^\eta(k)), \tag{A-8}$$

which will make the operator response $D^\eta(k)$ close to ik and close to equiripple simultaneously. This error criterion is identical to the group-velocity criterion introduced by Holberg,(1987),

$$\varepsilon^\eta_{gr}(k) = \varepsilon^\eta(k) + k\partial_k\varepsilon^\eta(k). \tag{A-9}$$

The chosen procedure is to minimize the error functional $\mathcal{E}^\eta_L$,

$$\mathcal{E}^\eta_L = [\int_{k=0}^{K_m} dk(\frac{1}{i}\partial_k D^\eta(k) - 1)^n + w(\sum_{l=-L}^{L}\alpha^\eta_l)]^2, \tag{A-10}$$

where

$$\frac{1}{i}\partial_k D^\eta(k) = \sum_{l=-L}^{L}\alpha^\eta_l(l-\eta)e^{ik(l-\eta)\Delta x}. \tag{A-11}$$

The term proportional to the weight w in equation (A-10) ensures that the sum of all derivative operator coefficients is zero. This constraint must be implemented to give operators, which when applied to constant functions give a derivative of zero as result, independently of the phase shift. The best w value was found to be typically 5×10^{-4} and the best value of n was found to be 4. An additional constraint is that the relative group velocity error $\varepsilon^\eta_{gr}(k)$ is less than the tolerance E_m for all wavenumbers up to the maximum wavenumber K_m. The coefficients α^η_l are the variables in this standard least square problem. A solution is accepted when K_m can not be increased further with the given E_m. The value of E_m is of order 10^{-2} - 10^{-3}.

Appendix B: Monopole and shift operator.

The monopole operator needed in the source term of the wave equation or in the implementation of the boundary condition is the Dirac delta function,

$$\delta(x - x_s). \tag{B-1}$$

The Dirac delta function also defines the convolutional shift operator $s_x^{\delta x}$,

$$\begin{aligned} \phi(x + \delta x) &= \int_{-\infty}^{\infty} dx' \{\delta(x' - \delta x)\}\phi(x + x') \\ &= s_x^{\delta x} * \phi(x). \end{aligned} \tag{B-2}$$

Assume that this operator can be bandlimited and is to be used on a regularly sampled function with sampling interval Δx. Let $x = i\Delta x$ with i integer. Let $\delta x = \eta \Delta x$ with η real number such that $-0.5 \leq \eta \leq 0.5$. The discretized version of $s_x^{\delta x}$ is denoted S_x^{η},

$$\begin{aligned} \phi(j\Delta x + \eta \Delta x) &= S_x^{\eta}\phi(j\Delta x) \\ &= \sum_{l=-L}^{L} \Delta x[\tilde{\delta}(l\Delta x - \eta \Delta x)]\phi(j\Delta x + l\Delta x) \\ &= \sum_{l=-L}^{L} \beta_l^{\eta} \phi_{j+l}. \end{aligned} \tag{B-3}$$

The Fourier response of S_x^{η} is,

$$S^{\eta}(k) = \sum_{l=-L}^{L} \beta_l^{\eta} e^{ik(l-\eta)\Delta x}. \tag{B-4}$$

Let the response of $S^{\eta}(k)$ be represented by,

$$S^{\eta}(k) = 1 + \varepsilon^{\eta}(k) \tag{B-5}$$

where $\varepsilon^{\eta}(k)$ is the relative error in frequency response of the operator S_x^{η}. The derivative of the frequency response of $S^{\eta}(k)$ is,

$$\partial_k S^{\eta}(k) = \partial_k \varepsilon^{\eta}(k). \tag{B-6}$$

The group velocity criterion can be used for the shift operator as for the derivative operator discussed in Appendix A. If it is required that $S^{\eta}(k)$ is as close as possible to 1 and that the derivative of $S^{\eta}(k)$ with respect to k is as close to 0 as possible then,

$$\min(S^{\eta}(k) - 1 + k\partial_k S^{\eta}(k)) = \min(\varepsilon^{\eta}(k) + k\partial_k \varepsilon^{\eta}(k)) = \min(\varepsilon_{gr}^{\eta}(k)), \tag{B-7}$$

which will make the operator response $S^\eta(k)$ close to equiripple.

The error functional $\mathcal{E}_L^\eta$ is then,

$$\mathcal{E}_L^\eta = [\int_{k=0}^{K_m} dk(S^\eta(k) - 1 + k\partial_k S^\eta(k))^n + w(\sum_{l=-L}^{L} \beta_l^\eta - 1)]^2 \tag{B-8}$$

where,

$$S^\eta(k) - 1 + k\partial_k S^\eta(k) = \sum_{l=-L}^{L} \{\beta_l^\eta [1 + ik(l-\eta)\Delta x] e^{ik(l-\eta)\Delta x}\} \quad - 1. \tag{B-9}$$

The term proportional to w in equation (B-8) ensures that the sum of all shift operator coefficients is equal to 1. This constraint must be implemented to give operators, which when applied to a constant function give the constant function as result independently of phase shift. The optimized coefficients β_l^η are found with the same least square procedure as the optimized α_l^η coefficients discussed in Appendix A.